Nanoscale

ROYAL SOCIETY OF CHEMISTRY

COMMUNICATION

View Article Online
View Journal | View Issue

Cite this: *Nanoscale*, 2025, **17**, 22122

Received 15th July 2025,
Accepted 3rd September 2025

DOI: 10.1039/d5nr02999f

rsc.li/nanoscale

Rigid support–molecular regulation–interface reinforcement synergistic strategy enables PEO-based electrolytes for solid-state lithium batteries

Yingtai Zhao,†[a,b,c] Xiangping Feng,†[a,b,c] Xin Sun,[a,b,c] Lei Zhang,*[d] Zhishuang Song,[a,b,c] Jinzhu Zhao,[e] Zhiyuan Wang,[a,b,c] Runguo Zheng,*[a,b,c] Hongyu Sun *[b] and Yanguo Liu*[a,b,c]

Poly(ethylene oxide) (PEO)-based solid polymer electrolytes have broad application prospects due to their flexibility, high lithium salt solubility, and low cost. However, low ionic conductivity, low Li^+ transference number, poor electrochemical stability, and inadequate mechanical strength restrict their application in solid-state lithium batteries (SSLBs). Herein, a composite solid-state electrolyte (CSE), PEO@GFC-15, is prepared using a simple and scalable solution casting method, incorporating glass fiber cloth (GFC) and $Li_{6.4}Al_{0.1}La_3Zr_{1.7}Ta_{0.3}O_{12}$ (LALZTO) particles. LALZTO can enhance Li^+ transport kinetics by increasing the amorphous region, constructing a Li–O–C dynamic coordination network, and providing more free Li^+. It can also promote the decomposition of lithium salt to generate abundant LiF and fix $TFSI^-$, enhancing interface stability, with the oxidation potential increasing to 5.2 V. The high elastic modulus of GFC and the strong hydrogen bond network endow PEO@GFC-15 with good flexibility. Additionally, the three-dimensional rigid network and non-flammable inorganic LALZTO particles improve its thermal stability. Therefore, the Li plating/stripping stability and electrochemical performance of SSLBs are effectively enhanced by the rigid support–molecular regulation–interface reinforcement synergistic modification strategy. This work provides practical insights for the development of high-performance SSLBs.

1. Introduction

Lithium-ion batteries (LIBs) have been widely employed in various fields, including electronic devices, new energy vehicles, energy storage systems, aerospace, and military applications, due to their high energy density (150–300 Wh kg^{-1}), long cycle life (>1000 cycles), low self-discharge rate, and lack of a memory effect.[1] However, several critical issues need to be addressed urgently. First, the flammability (such as low flash points of carbonate solvents) and leakage-prone characteristics of the liquid electrolyte increase the risk of battery thermal runaway and fire. Second, an unstable solid electrolyte interface (SEI) is likely to form at the liquid electrolyte/electrode interface, leading to interface side reactions and rapid capacity fading. Moreover, liquid electrolytes limit the application of a Li metal anode because Li dendrite growth can cause cell short circuits. Finally, liquid electrolytes are highly viscous at low temperatures (such as −20 °C) and easily volatilise at high temperatures (such as 60 °C), thereby restricting the operating temperature window of LIBs.

Fortunately, substituting solid-state electrolytes (SSEs) for traditional liquid electrolytes can significantly improve the safety, energy density, cycle life, and interface stability of cells.[2] Inorganic ceramic electrolytes (such as garnet-type $Li_7La_3Zr_2O_{12}$, LLZO) enable the long-term stable cycling of cells because of their good ionic conductivity, thermal stability, and (electro)chemical stability. However, ceramic brittleness and conventional powder pressing and sintering processes limit their use in fabricating large-sized and ultra-thin electrolyte membranes (typically thicker than 500 μm after sintering). This thickness constraint reduces the energy density of solid-state lithium batteries (SSLBs). In contrast, flexible polymer electrolytes (such as poly(ethylene oxide), PEO) are easy to prepare into large and thin solid electrolyte membranes (about 50 μm thickness) due to excellent processability, which enables conformable electrolyte/electrode interface contact. In addition, the repeating $-CH_2-CH_2-O-$ units in PEO chains provide excellent lithium salt solubility and promote the for-

[a]*School of Materials Science and Engineering, Northeastern University, Shenyang 110819, China. E-mail: zhengrunguo@126.com, lyg@neuq.edu.cn*
[b]*School of Resources and Materials, Northeastern University at Qinhuangdao, Qinhuangdao 066004, China. E-mail: hyltsun@gmail.com*
[c]*Key Laboratory of Dielectric and Electrolyte Functional Material Hebei Province, Northeastern University at Qinhuangdao, Qinhuangdao 066004, China*
[d]*Key Laboratory of Magnetic Materials and Devices, and Zhejiang Province Key Laboratory of Magnetic Materials and Application Technology, Ningbo Institute of Materials Technology and Engineering, Chinese Academy of Sciences, Ningbo 315201, China. E-mail: zhanglei1281@163.com*
[e]*Department of Material Engineering, Hebei Construction Material Vocational and Technical College, Qinhuangdao 066002, China*
†The authors contribute equally.

mation of metal-lithium salt composites.[3–5] The PEO chains in the flexible macromolecular structure also enable dynamic movement, facilitating Li^+ transport. However, the semi-crystalline property of PEO, especially in crystalline regions, hinders effective Li^+ transport, resulting in a low Li^+ transference number (t_{Li^+}) and low ionic conductivity (generally between 10^{-8} and 10^{-6} S cm^{-1}) at room temperature.[6–8] Recently, various strategies have been developed to enhance the Li^+ transport capability of PEO-based electrolytes. For example, Huang *et al.*[9] designed a high-concentration lithium salt to regulate anion adsorption behavior, optimize cation–anion co-transport, and increase t_{Li^+} to 0.68 and ion conductivity to 1.02×10^{-4} S cm^{-1}. Hu *et al.*[10] introduced a Li–Al–O Lewis acid–base pair to destroy the crystalline structure of the PEO chains and create uniform Li^+ transport channels, enhancing the ionic conductivity to 3.5×10^{-4} S cm^{-1}.

Novel electrolytes require high ionic conductivity coupled with robust thermal stability, tolerance to high voltage, mechanical flexibility, and interfacial compatibility.[11] At first, high-voltage stability indicates an expanded electrochemical stability window, which is favorable for improving the compatibility and safety of the electrolyte. Wu *et al.*[12] enabled the cell to run stably at 4.3 V for 200 cycles by adding LiBOB to the electrolyte. Zhang *et al.*[13] designed a locally high-concentration electrolyte to reduce viscosity while maintaining the advantage of high salt concentration, improving the oxidative stability of PEO at high voltages. In addition, electrolyte flexibility is crucial for cell performance. Song *et al.*[14] increased the mechanical modulus of a PEO-based electrolyte to 20 MPa by introducing Li_6PS_5Cl sulfide, significantly suppressing Li dendrite penetration. Li *et al.*[15] achieved an elongation at break of 200% by utilizing SP and polyurethane (PU) to form an interpenetrating network, effectively prolonging cell cycling life. Finally, a stable interface is also critical to the long-term cycle stability of cells. Chen *et al.*[16] successfully generated *in situ* a dense LiF layer on the Li metal surface by introducing $LiPO_2F_2$ additives, suppressing Li dendrite growth and lowering interface impedance. Zhang *et al.*[17] established a stable interface and realized long-term stable work by dispersing LLZO nanoparticles in PEO chains. To optimize lithium growth, 3D current collectors increase deposition/stripping of active sites, reduce surface current density, and provide stable nucleation sites.[18] Notably, remarkable advances have been achieved in each of the above-mentioned directions of improvement. Nonetheless, the challenge lies in integrating these requirements to design a novel electrolyte with high ionic conductivity, a wide electrochemical stability window, good flexibility, and interface stability.

In this work, an organic–inorganic composite solid electrolyte (CSE, PEO@GFC-15) was prepared using a simple and scalable solution casting method. The addition of $Li_{6.4}Al_{0.1}La_3Zr_{1.7}Ta_{0.3}O_{12}$ (LALZTO) particles can enhance Li^+ transport capacity by reducing PEO crystallinity to increase amorphous regions, creating a dynamic Li–O–C coordination network, and providing numerous movable Li^+ ions. The ionic conductivity and Li^+ transference number are 2.89×10^{-5} S cm^{-1} and 0.77, respectively. Moreover, LALZTO can broaden the electrochemical stability window by promoting LiTFSI decomposition to produce abundant LiF and fixing $TFSI^-$ on the PEO chains. The oxidation potential is notably increased to 5.2 V. The introduction of GFC with a high elastic modulus and the strong hydrogen bond network between PEO and LALZTO enables an electrolyte with good flexibility. The three-dimensional rigid network and non-flammable inorganic LALZTO particles efficiently improve the thermal stability of the electrolyte. Furthermore, PEO@GFC-15 can establish a stable electrode/electrolyte interface by modulating Li plating/stripping behavior and minimizing HTFSI generation. Therefore, the cell performance could be greatly improved by the rigid support–molecular regulation–interface reinforcement synergistic modification strategy.[17–21]

2. Experimental section

2.1 Preparation of LALZTO particles

Garnet-type cubic phase LALZTO particles were synthesized using previously reported methods.[22,23] To be specific, $LiOH{\cdot}H_2O$ (Aladdin, 98%), La_2O_3 (Aladdin, 99.99%, preheated in air at 950 °C for 8 h to remove CO_2 and H_2O), ZrO_2 (Aladdin, 99%), Al_2O_3 (Aladdin, 99.99%), and Ta_2O_5 (Aladdin, 99.5%) were weighed according to the stoichiometric ratio. An excess of 10 wt% $LiOH{\cdot}H_2O$ was added to compensate for lithium loss at high-temperature calcination. The powder was mixed with isopropanol and ball-milled at 400 rpm for 6 h. After drying at 80 °C for 12 h, the dried powder was calcined at 950 °C for 6 h. The collected powder was ball-milled at 400 rpm for 12 h to further refine the particles. The cubic phase LALZTO particles were obtained after drying at 80 °C for 12 h. The prepared LALZTO particles were stored in an argon-filled glove box with low O_2 and H_2O content of <0.01 ppm for future use.

2.2 Preparation of CSEs

CSEs were prepared by the solution casting method. PEO (M_w = 600 000) and LiTFSI were vacuum-dried at 60 °C for 12 h to remove moisture, and weighed in a molar ratio of EO : Li = 18 : 1. Then, 10 mL of acetonitrile solution was added and stirred for 6 h. The PEO-*x* solution was obtained by introducing *x* wt% (*x* = 0, 10, 15, and 20) LALZTO particles into the mixed solution. The GFC was ultrasonically cleaned sequentially with acetone, ethanol, and deionized water (0.5 h each), and then placed flat on a polytetrafluoroethylene (PTFE) plate after drying. 10 μL of PEO-*x* solution was used to fill the GFC. The CSEs (PEO@GFC-*x*, *x* = 0, 10, 15, and 20) were obtained by vacuum-drying at 80 °C for 12 h with volatile organic solvents. In addition, a pure PEO electrolyte contains only PEO and LiTFSI, without GFC or LALZTO particles. All operations were performed in a glove box under argon atmosphere (H_2O < 0.01 ppm, O_2 < 0.01 ppm).

2.3 Battery assembly

A CR2032-type Li symmetric battery, Li|CSE|Li cell, was assembled in the order of anode shell, foam nickel, Li foil,

CSE, Li foil, foam nickel, and cathode shell from bottom to top. The stainless steel (SS)|CSE|Li cell was assembled by replacing the Li foil with SS foil on the cathode side. The SS|CSE|SS cell was assembled by replacing the Li foil with SS foil on both the cathode and anode sides. The SSLBs were assembled into CR2032 cells. The $LiFePO_4$ (LFP) or $LiNi_{0.5}Co_{0.2}Mn_{0.3}O_2$ (NCM523) cathodes were prepared by mixing 80 wt% active materials, 10 wt% carbon black and 10 wt% polyvinylidene fluoride (PVDF) in *N*-methyl-2-pyrrolidone (NMP) solution. The obtained slurry was cast homogeneously onto a carbon-coated aluminium foil and dried at 120 °C for 12 h in a vacuum oven. The average loading mass of the active material was 2.0 mg cm^{-2}. The cell was assembled in the order of anode shell, nickel foam, Li foil, CSE, cathode plate, nickel foam, and cathode shell from bottom to top. All preparation steps were performed in a glove box under argon atmosphere (H_2O < 0.01 ppm, O_2 < 0.01 ppm).

2.4 Materials characterization

The phase and crystal structure were determined by X-ray diffraction (XRD, Rigaku Smart Lab). Cu Kα radiation (λ = 1.5406 Å) was selected as the radiation source, and the scanning rate was 5° min^{-1}. The micro-morphology was observed using field emission scanning electron microscopy (SEM, ZEISS SUPRA55 SAPPHIRE, 15 kV). The elemental distribution was obtained with an energy dispersive spectrometer (EDS). Surface chemical composition analysis was characterized under Ar protection by X-ray photoelectron spectroscopy (XPS, American Thermo Fisher Scientific ESCALAB 250Xi) with an Al Kα source. The C 1s peak at 284.8 eV was selected for energy calibration of parameters. Thermogravimetric analysis (TGA) experiments were carried out on Mettler Toledo TGA/DSC 3+ equipment at a ramp rate of 5 °C min^{-1} from 30 to 800 °C under an N_2 atmosphere. Fourier transform infrared (FTIR) spectroscopy was performed under attenuated total reflectance (ATR)-FTIR mode using a Thermo Scientific Nicolet iS5.

2.5 Electrochemical measurements

Electrochemical impedance spectroscopy (EIS) was carried out on a Zahner Pro electrochemical working station in a frequency range of 7 MHz to 1 Hz with a voltage amplitude of 10 mV. The ionic conductivity (σ) of GI from 25 to 80 °C was tested with an SS|CSE|SS cell. The specific σ values were calculated using the following equation:

$$R = d/(\sigma S)$$

where d is the CSE thickness, R is the resistance value, and S is the area of stainless steel. The activation energy (E_a) was calculated with the following equation:

$$\sigma T = A \exp(-E_a/kT)$$

where A is a pre-exponential factor, T is the absolute temperature, and k refers to the Boltzmann constant.

Linear sweep voltammetry (LSV) was conducted from 2 to 7 V at a scan rate of 1 mV s^{-1} with a CHI760E electrochemical workstation. The Li^+ transference number was determined by a potentiostat polarization method in Li symmetric cells and calculated using the following equation:

$$t_{Li^+} = [I_s(\Delta V - I_0R_0)]/[I_0(\Delta V - I_sR_s)]$$

where ΔV is the polarization voltage (10 mV), R_0 and I_0 are the resistance and current before polarization, and R_s and I_s are the resistance and current after polarization, respectively.

The direct current (DC) polarization technique was applied with a voltage of 1 V and a holding time of 3600 s. The interface resistance of the Li symmetric cell was calculated based on dividing the experimentally derived resistance by two and then normalizing it to the contact interface area. The galvanostatic Li stripping/plating behaviour at 0.1 mA cm^{-2} for 0.5 h per step was evaluated using a LAND test system. The time control mode is used to test critical current density (CCD), which is performed with a fixed time length of 1 h in each cycle and gradually increasing a fixed current density from 0.1 mA cm^{-2}. The SSLBs were charged/discharged on the LAND test system in the voltage ranges 2.5–3.8 V for LFP and 3.0–4.3 V for NCM523. The theoretical specific capacities are 170 and 170 mAh g^{-1} for LFP and NCM523, respectively.

3. Results and discussion

3.1 Preparation and characterization of CSEs

The detailed process of CSE preparation and action mechanism are illustrated in Fig. 1. PEO@GFC-15 is prepared by a simple and scalable solution casting method, and exhibits rapid Li^+ transport capability, wide electrochemical stability window, good flexibility, and improved thermal stability (Step 1). The introduced LALZTO particles can reduce PEO crystallinity, create a dynamic Li–O–C coordination network, and generate abundant moveable Li^+, enhancing the Li^+ transport capability within the electrolyte. LALZTO can also promote LiTFSI decomposition to form large amounts of LiF and fix $TFSI^-$ on the PEO chain, broadening the electrochemical stability window of the electrolyte. Moreover, the high elastic modulus of GFC and the strong hydrogen bond network endow the electrolyte with good flexibility. The three-dimensional rigid network and non-flammable inorganic LALZTO particles improve the thermal stability. PEO@GFC-15 demonstrates good interface stability during cycling (Step 2). At the anode side, fast Li^+ conductivity and good flexibility of the electrolyte and stable interface capability of the LiF reduce interface resistance and suppress Li dendrite growth, resulting in stabilized Li plating/stripping behavior. At the cathode side, TFSI anions, immobilized by PEO chains, together with the H^+-capturing ability of LiF, suppress HTFSI generation, thereby constructing a low-resistance and stable cathode/electrolyte interface. Thanks to this, the electrochemical performance of SSLBs is significantly enhanced.

As shown in Fig. S1, PEO-0 appears as a clear and transparent solution, whereas PEO-10/15/20 appears as a milky-white dispersion due to the presence of LALZTO particles. The surface and cross-sectional microstructure of the PEO electro-

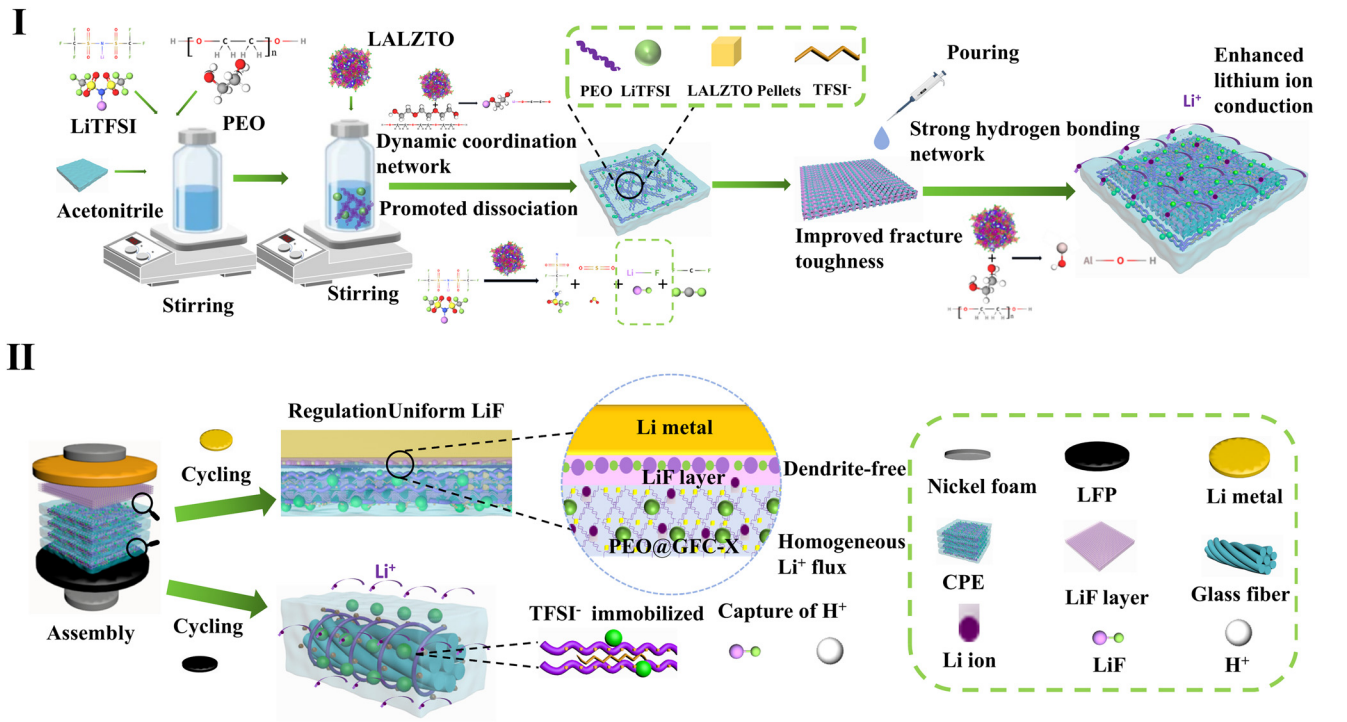

Fig. 1 Schematic illustration of PEO@GFC-15 preparation I and roles II.

lyte was visualized by SEM. As shown in Fig. 2a and b, the thickness of the PEO electrolyte is ~25.3 μm, and the surface is rough with several micropores. The formation of micropores is attributed to rapid solvent evaporation during preparation, which is a common feature in solution casting methods. Furthermore, high surface roughness indicates more crystalline regions within the PEO electrolyte. Li^+ migration occurs mainly in the amorphous region through the movement of polymer segments, whereas the crystalline region would hinder Li^+ transport. To address the above issues, GFC is introduced into the PEO electrolyte. As shown in Fig. 2c and d, GFC shows a distinct fiber weave structure with an average thickness of ~50 μm. The surface of a single fiber is smooth and flat. After introducing GFC, the surface micropores nearly disappeared, and the GFC framework was uniformly incorporated into the PEO matrix (Fig. 2e).

Fig. 2f–h shows the surface and cross-sectional microstructures of PEO@GFC-10, PEO@GFC-15, and PEO@GFC-20. Combined with PEO@GFC-0, the thickness of these CSEs ranges from 60 to 70 μm. However, all surfaces display wrinkling, attributed to capillary forces generated as the solution penetrates the gaps between GFC fibers. With increasing LALZTO particle content, the surface of the CSE gradually becomes smoother, reflecting a more uniform dispersion of the filler and the formation of continuous PEO crystallites. The presence of LALZTO particles strengthens the interactions between the filler and the matrix, facilitating bridging between both filler–filler and filler–matrix interfaces. These effects significantly improve the fracture toughness of the CSE. When the content of LALZTO increases to 20 wt%, local agglomeration of particles occurs on the surface. This is because a LALZTO particle exhibits high surface energy, leading to difficult dispersion.[24,25] The agglomeration of LALZTO particles could weaken the suppression of PEO crystallization, impeding rapid Li^+ transport. The surface of PEO@GFC-15 shows optimal flatness in Fig. 2f–h. The elements C, N, F, Si, S, O, La, Zr, Ta, and Al are uniformly distributed (Fig. 2i).

The crystal structure of the CSEs was analyzed with XRD patterns. As shown in Fig. 3a, the diffraction peak intensities of PEO electrolytes at 19.3° and 23.7° exhibit a decrease–increase–decrease trend. Initially, oxygen-containing functional groups on the surface of GFC form hydrogen bonds with the ether oxygens in PEO, which disrupts the chain alignment and reduces crystallinity, leading to a lower peak intensity and narrower peak width compared to pure PEO.[26] Upon the addition of LALZTO, oxygen vacancies and metal ions polarize the PEO chains, enhancing their alignment and crystallinity. However, as the content of LALZTO increases further, the chain order is disrupted, resulting in a reduction in crystallinity.

As shown in Fig. 3b, the chemical interactions among LALZTO, PEO, and LiTFSI were investigated by FTIR. In the range of 3500–3700 cm^{-1}, the broad peak in PEO@GFC-0 is attributed to the free hydroxyl group (–OH). After introducing LALZTO, this broad peak shifts to 3200–3500 cm^{-1}, with increased peak intensity and width. This is due to the strong hydrogen bond network formed by coordinate bonding between the Lewis acidic sites (such as Al) on LALZTO and the –OH in PEO chains, resulting in reduced electron density for the O–H bond.[27–29] The characteristic absorption peaks at 2880 and 1094 cm^{-1} are assigned to the stretching vibrations

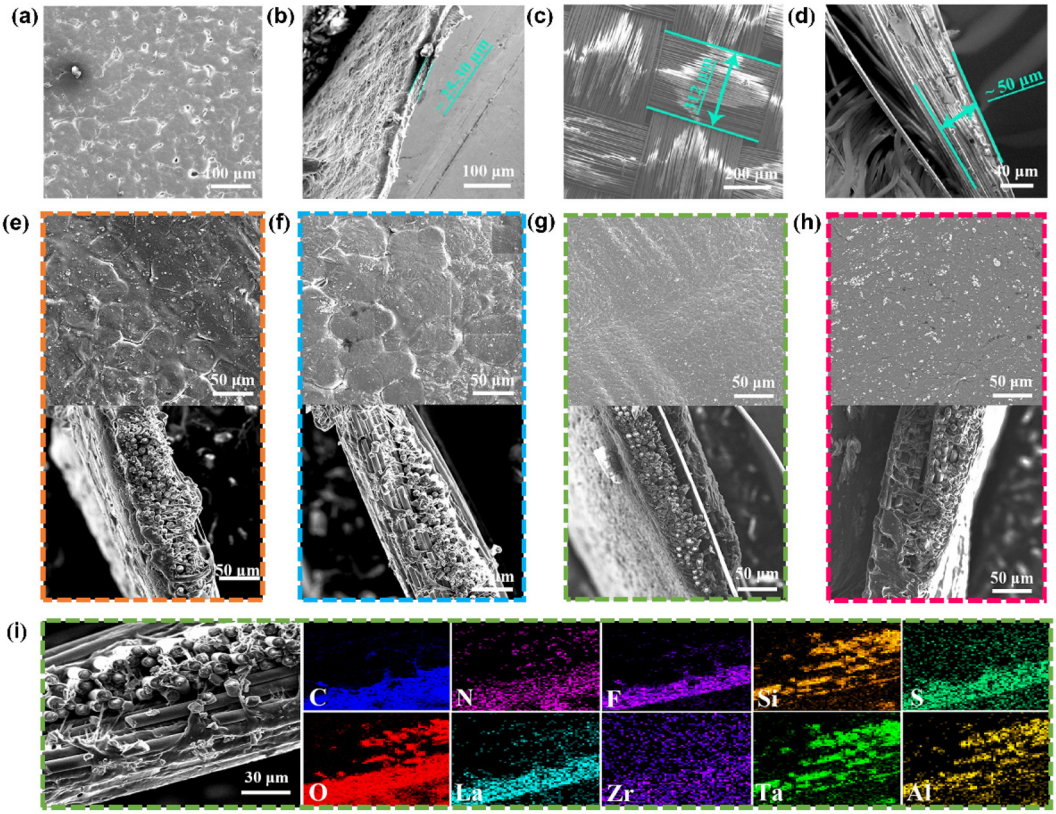

Fig. 2 Morphology of CSEs. SEM images of (a and b) PEO electrolyte, (c and d) GFC, (e) PEO@GFC-0, (f) PEO@GFC-10, (g) PEO@GFC-15, and (h) PEO@GFC-20. (i) EDS mapping analysis of PEO@GFC-15.

of the C–H bond and C–O–C bond in PEO, respectively. As the content of LALZTO particles increases, the peak of C–O–C bond stretching vibration is redshifted to 1070 cm^{-1}, and the peak symmetry is enhanced. This can be ascribed to the metal elements in LALZTO bonding with ether oxygen groups through coordination covalent interactions, which increase the polarity of the C–O–C bond and change its vibrational dipole moment. The characteristic absorption peaks at 1284, 1242, and 960 cm^{-1} are assigned to the bending vibrations of the $-CH_2$ group in PEO, and peaks in the range of 1400–1600 cm^{-1} are assigned to vibrations of the C═O/C═N bond of the benzene ring structure in GFC. The above results reveal that stable hydrogen bonds and coordination bonds are formed between LALZTO and PEO, enhancing polymer chain movement and lowering PEO crystallinity, as well as optimizing Li^+ transport performance. In addition, CSEs with LALZTO particles show a weak new vibration peak at 865 cm^{-1} for the C–N bond (Fig. 3c). The formation of a C–N bond suggests that interaction exists between the C atom in PEO and the N atom in LiTFSI. This is because LALZTO can promote the dissociation of Li^+–$TFSI^-$ ion pairs and fix $TFSI^-$ on the polymer chain.[30,31] Therefore, the introduction of LALZTO increases the free Li^+ concentration and constructs Li^+ transport pathways, assisting in facilitating the Li^+ migration capability.

The chemical composition and electronic state of the PEO electrolyte, PEO@GFC-0, and PEO@GFC-15 were investigated by XPS. As shown in Fig. 3d, the Li–O bond energy of PEO@GFC-15 is lower than that of PEO or PEO@GFC-0. This could be because of the formation of a dynamic Li–O–C coordination network through partial electron cloud sharing between Li^+ and C–O–C bonds in PEO after introducing LALZTO, lowering the binding energy of the Li–O bond. The peaks at 283.4 eV and 284.8 eV in the C 1s spectrum are attributed to C–H bonds and C–C bonds, respectively (Fig. 3e). Moreover, the peaks at 532.2 and 531.6 eV in the O 1s spectrum are attributed to the O–H bond and C–O bond, respectively (Fig. 3f).

Due to the dynamic Li–O–C coordination network between LALZTO and PEO, the peak intensity of C–O bond is weakened in PEO@GFC-15. These results indicate that LALZTO can induce PEO chain disorder, promote free chain movement in the amorphous region, and facilitate local Li^+ migration. As shown in Fig. 3g, the peaks at 684.5 and 688.3 eV in the F 1s spectrum are attributed to $TFSI^-$ in LiTFSI and LiF, respectively. LiF is generated by the decomposition of LiTFSI, and it is beneficial for forming a stable interlayer to suppress Li dendrite growth and enable uniform Li deposition.[32–34] Notably, the LiF content is highest in PEO@GFC-15, indicating that LALZTO can facilitate the decomposition of LiTFSI. Overall, the strong interactions among LALZTO, PEO, and LiTFSI not only enhance Li^+ transport capability but also assist in forming a stable interlayer.

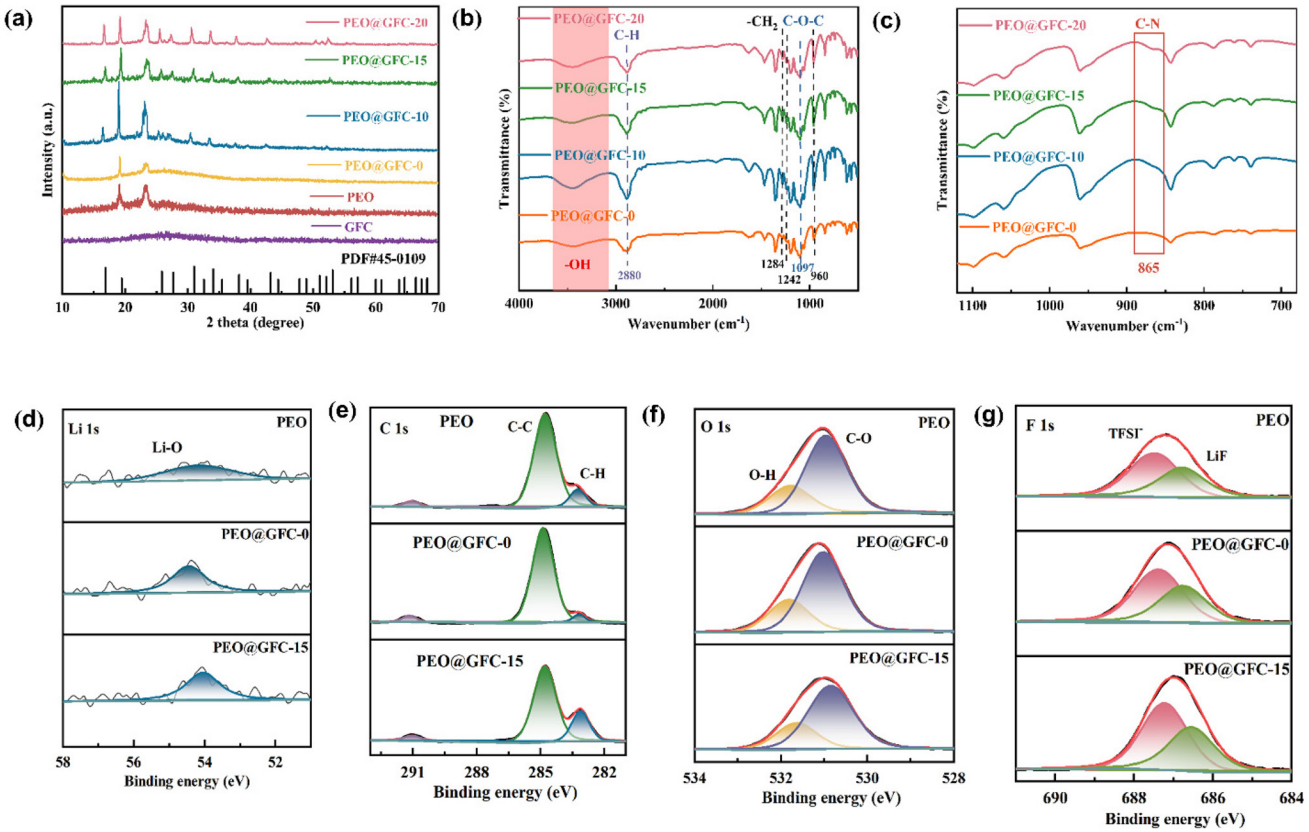

Fig. 3 Characterization of CSEs. (a) XRD patterns of GFC, PEO, PEO@GFC-0, PEO@GFC-10, PEO@GFC-15, and PEO@GFC-20. (b and c) FTIR of PEO@GFC-0, PEO@GFC-10, PEO@GFC-15, and PEO@GFC-20. (d) Li 1s, (e) C 1s, (f) O 1s, and (g) F 1s core levels for PEO, PEO@GFC-0, and PEO@GFC-15.

3.2 Performance analysis of CSEs

Ionic conductivity is a critical parameter for evaluating electrolyte performance and has a significant impact on battery output power and cycle life. As PEO-based SSEs generally exhibit high resistance (>1 MΩ) at room temperature,[35,36] EIS experiments on CSE were performed at 60 °C. As shown in Fig. 4a, b and Fig. S2, the ionic conductivities of PEO electrolyte, PEO@GFC-0, PEO@GFC-10, PEO@GFC-15, and PEO@GFC-20 are 1.49×10^{-5}, 1.60×10^{-5}, 2.48×10^{-5}, 2.89×10^{-5}, and 2.55×10^{-5} S cm^{-1}, respectively, with migration activation energies of 0.67, 0.65, 0.63, 0.50, and 0.63 eV, respectively.

With increasing LALZTO content, the ionic conductivity first increases and then decreases, while the migration activation energy first decreases and then increases, indicating that introducing appropriate amounts of LALZTO can improve Li^+ conduction. On the one hand, LALZTO lowers PEO crystallinity and enlarges the amorphous phase region, facilitating Li^+ migration. On the other hand, the dynamic Li–O–C coordination network between LALZTO and PEO facilitates Li^+ migration by reducing the migration barrier through electron cloud sharing. The ether oxygen (–O–) bridges Li^+ and the adjacent –CH_2–, enabling electron cloud sharing among the three entities. This interaction weakens electron donation from O to Li^+, thereby reducing the Li–O bond strength and lowering the migration barrier.[37] XPS analysis shows that the Li–O binding energy shifts to higher binding energies in the presence of LALZTO/GFC, consistent with the electron cloud sharing mechanism.

However, as the LALZTO content increases to 20 wt%, particle agglomeration causes phase separation between particle and matrix, obstructing Li^+ transport. Moreover, high LALZTO content will limit the random movement of PEO chains and damage the Li–O–C dynamic coordination network, increasing the tortuosity of Li^+ migration pathways. Based on this, PEO@GFC-15 shows optimal ionic conductivity and migration activation energy.

The Li^+ transference numbers for the CSEs were measured using electrochemical impedance spectroscopy (EIS) and the DC polarization method. As shown in Fig. 4c–h, the Li^+ transference numbers for PEO electrolyte, PEO@GFC-0, PEO@GFC-10, PEO@GFC-15, and PEO@GFC-20 are 0.214, 0.251, 0.425, 0.793, and 0.558, respectively. With increasing LALZTO content, the Li^+ transference number also first increases and then decreases. Similarly, appropriate amounts of LALZTO particles can lower the Li^+ migration energy barrier, increasing the number of movable Li^+. Furthermore, LALZTO

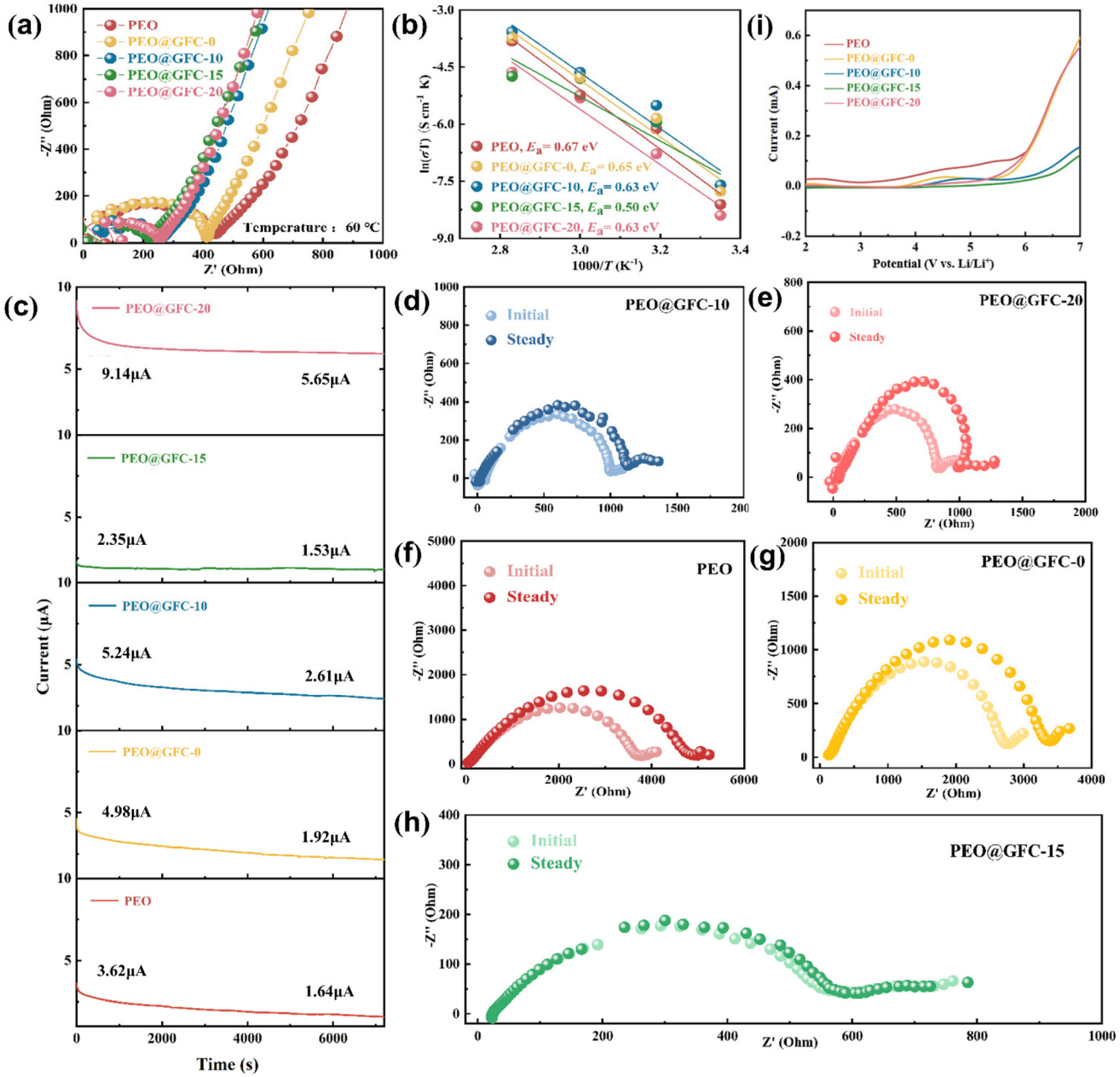

Fig. 4 Performance of CSEs. (a) Nyquist plots, (b) Arrhenius plots, (c) current–time curves, and (i) LSV curves of PEO, PEO@GFC-0, PEO@GFC-10, PEO@GFC-15, and PEO@GFC-20. Nyquist plots before and after polarization of (d) PEO, (e) PEO@GFC-0, (f) PEO@GFC-10, (g) PEO@GFC-15, and (h) PEO@GFC-20.

can promote LiTFSI decomposition to generate more free Li^+, and fix $TFSI^-$ on the polymer chains. However, when the LALZTO content is high, particle agglomeration and disruption of the Li–O–C dynamic coordination network could decrease the number of movable Li^+. Accordingly, PEO@GFC-15 exhibits the highest Li^+ transference number. The oxidation potential of the CSEs was investigated using LSV. As shown in Fig. 4i, the PEO electrolyte displays an oxide reaction current at a low potential of 3.3 V, indicating poor electrochemical stability. After introducing GFC, the oxidation potential is increased to 3.8 V, which is attributed to the high-modulus rigid skeleton and surface –COOH/–OH groups suppressing interface side reactions.[38,39] When introducing 10 wt% LALZTO particles, the oxidation potential is further increased to 4.0 V, demonstrating that LALZTO is capable of suppressing the decomposition of PEO electrolyte. When the LALZTO content is increased to 15 and 20 wt%, the oxidation potentials are 5.2 and 5.0 V, respectively. Enhanced oxidation stability arises from the dual optimization of thermodynamic and dynamic properties. Specifically, Lewis acidic sites and oxygen vacancies on the LALZTO ceramic surface coordinate $TFSI^-$ anions. The resulting ion–dipole interaction restricts

$TFSI^-$ diffusion to the cathode surface, modifying the decomposition environment at the interface. Consequently, this leads to an improved oxidation decomposition potential and an expanded electrochemical stability window.[40] Therefore, PEO@GFC-15 displays optimal Li^+ transport capability and electrochemical stability (Table S1).

Besides, electrolyte flexibility also impacts the long-term cycle stability of cells. As shown in Fig. S3, the PEO electrolyte develops irreversible creases after bending and folding. In contrast, PEO@GFC-15 can rapidly recover to its original state after removal of the applied force, demonstrating good flexibility. Specifically, GFC promotes uniform stress distribution and suppresses plastic deformation through a three-dimensional rigid network formed *via* π–π stacking and covalent modification.

In addition, its high elastic modulus (~1 TPa) can limit the creep and glide of PEO chains, improving resilience. LALZTO can also rapidly release stress through a strong hydrogen bond network. Consequently, GFC and LALZTO jointly endow PEO@GFC-15 with good flexibility.

The thermal stability of CSEs was investigated by TGA. As shown in Fig. S4, for all samples, it decreased only slightly in the range of 30–100 °C due to evaporation of moisture. The PEO chain begins to decompose at 370 °C, and the curve drops quickly. When the temperature reaches 480 °C, the PEO chain is completely decomposed. Based on this, the residual mass percentages of PEO electrolyte, PEO@GFC-0, and PEO@GFC-15 are 4.7 wt%, 62.1 wt%, and 65.4 wt%, respectively. Compared with PEO@GFC-0, introducing LALZTO particles further increases the residual mass percentage. Thus, GFC and LALZTO together improve the thermal stability of PEO@GFC-15. Overall, PEO@GFC-15 possesses optimal Li^+ transport capability, electrochemical stability, flexibility, and thermal stability.

3.3 Modulation of Li plating/stripping behavior

Stable Li plating/stripping behavior is crucial for the practical application of SSLBs. The CSE/Li interface resistance was first investigated by EIS of Li symmetric cells. As shown in Fig. 5a, the interface resistance decreases to 228.28 Ω cm^2 as the LALZTO particle content increases to 15 wt%. This could be because abundant LiF generated by LALZTO alleviated interface side reactions and established a stable interface structure. However, with a further increase to 20 wt%, the interface resistance increases to 558.13 Ω cm^2, which could be attributed to the reduced interface contact area between the CSE and the Li anode due to agglomeration of LALZTO particles.

Then the CCD was tested under a time-constant model. CCD is defined as the lowest current density at which a cell short circuits because of Li dendrite penetration. As shown in Fig. 5b, the overpotential of the Li|PEO|Li cell suddenly rises at 0.3 mA cm^{-2}, leading to a short circuit. In contrast, the CCD for Li|PEO@GFC-0/10/15/20|Li cells was enhanced to 0.4, 0.5, 0.8, and 0.6 mA cm^{-2}, respectively. Among them, the Li|PEO@GFC-15|Li cell shows the highest CCD of 0.8 mA cm^{-2}, demonstrating that introducing GFC and LALZTO can strengthen Li dendrite growth suppressing capability. This is due to the excellent Li^+ transport capability and flexibility of PEO@GFC-15 and the stable interface capability of LiF.[41]

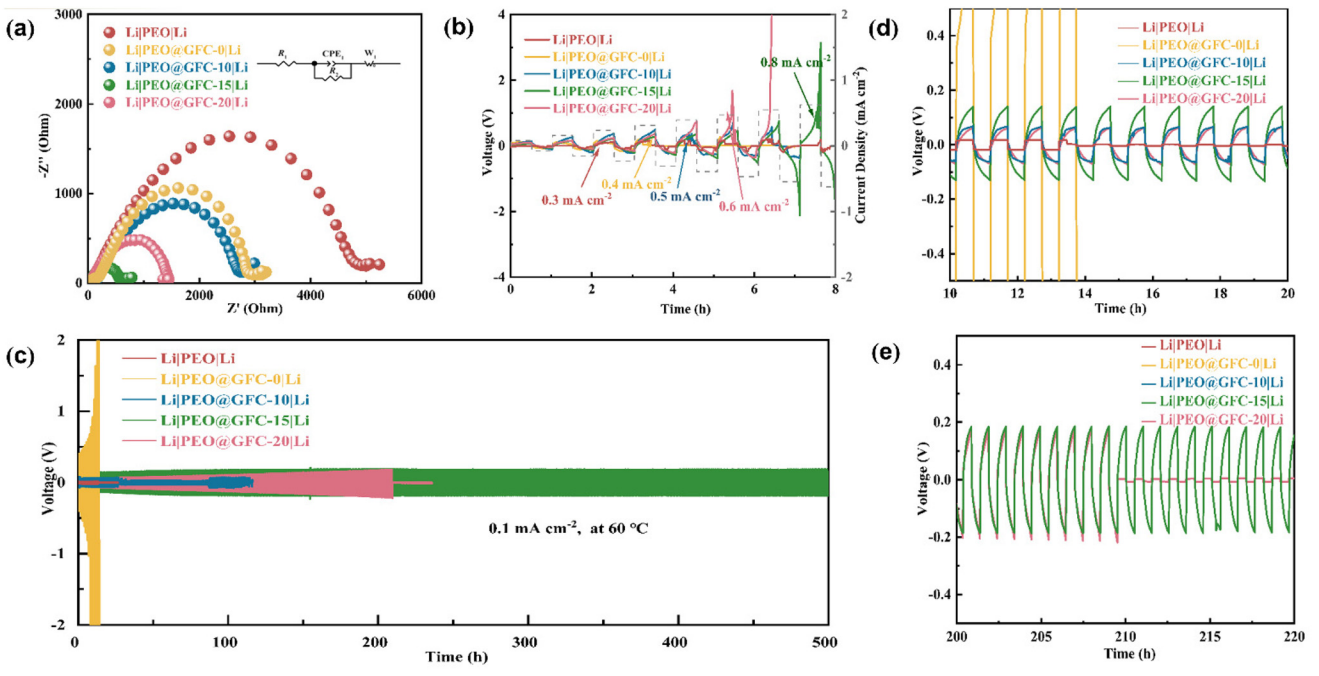

Fig. 5 Electrochemical performance of Li symmetric cells. (a) Nyquist plots, (b) CCD profiles, (c) Li plating/stripping cycling at 0.1 mA cm^{-2}, and (d, e) enlarged voltage profiles of Li|CSEs|Li cells.

To evaluate interface stability during repeated Li plating/stripping, prolonged cycling of the Li symmetric cell was carried out at 0.1 mA cm^{-2}. As shown in Fig. 5c–e, the Li|PEO|Li cell displays micro-short-circuiting in the initial cycle. After cycling for 10 h, the voltage suddenly dropped due to Li dendrite growth, leading to cell short-circuiting. Introducing GFC can rapidly promote uniform Li deposition. However, the cell voltage rises rapidly during the following cycles due to the development of an inhomogeneous interlayer, ultimately causing cell failure. The Li|PEO@GFC-15|Li cell shows stable cycling for 500 h with an overpotential of ~0.14 V, exhibiting impressive Li plating/stripping performance. This can be attributed to the superior Li^+ transport capability, flexibility, and abundant LiF of PEO@GFC-15, enabling reduced interface resistance, suppression of Li dendrite growth, and stabilization of the interface. Furthermore, Li|PEO@GFC-10|Li and Li|PEO@GFC-20|Li cells can also be cycled stably within 100 h. Notably, introducing excessive or insufficient LALZTO particles can both impair stable Li plating/stripping behavior. Specifically, insufficient Li^+ transport channels in PEO@GFC-10 lead to a soft short circuit during cycling. Li dendrites ultimately grow through the electrolyte, leading to complete short-circuiting of the Li|PEO@GFC-10|Li cell. For the Li|PEO@GFC-20|Li cell, the voltage (namely the interface resistance) is continuously increased due to agglomeration of LALZTO particles. The voltage drops dramatically and irreversibly until a hard short circuit occurs, displaying a linear response signal.

3.4 SSLBs performance

A pure polymer electrolyte is susceptible to oxide decomposition at the cathode side, and shows poor electrochemical stability, leading to significant degradation in cell performance. To evaluate the practical application performance of CSEs, LFP|CSEs|Li SSLBs were assembled. As shown in Fig. 6a, the LFP|PEO@GFC-15|Li cell exhibits outstanding rate performance. The discharge specific capacities are 155.8, 153.4, 151.9, and 146.6 mAh g^{-1} at current densities of 0.1, 0.2, 0.3, and 0.5C, respectively. As the current density returns to 0.1C, the discharge specific capacity returns rapidly to 152.3 mAh

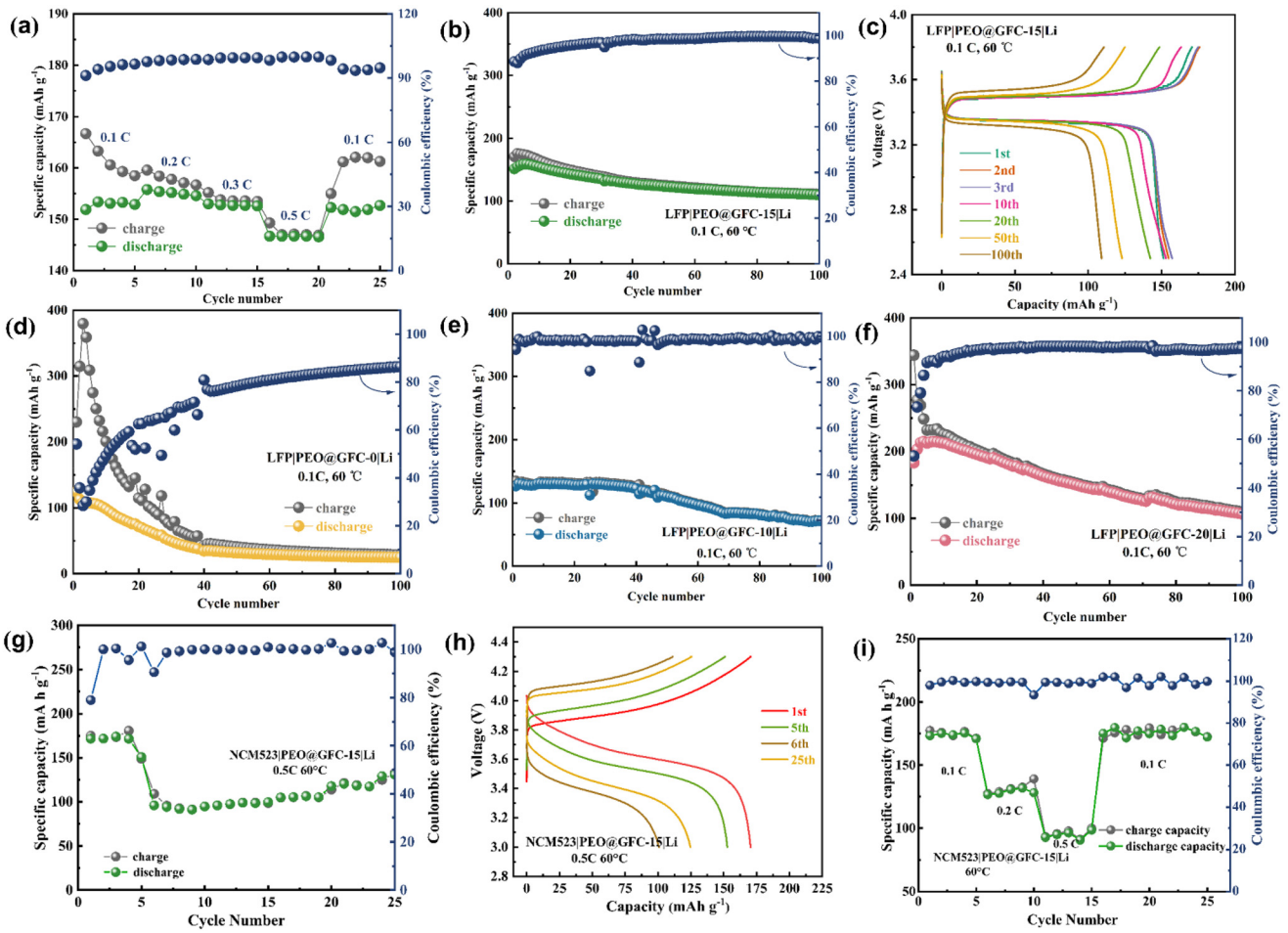

Fig. 6 Electrochemical performances of SSLBs. (a) Rate performance and (b) cycling performance at 0.1C of the LFP|PEO@GFC-15|Li cell. (c) The charge/discharge curves at different cycling stages of the LFP|PEO@GFC-15|Li cell at 0.1C. Cycling performance at 0.1C of (d) LFP|PEO@GFC-0|Li, (e) LFP|PEO@GFC-10|Li, and (f) LFP|PEO@GFC-20|Li cells. (g) Cycling performance at 0.5C and (h) the charge/discharge curves at different cycling stages of the NCM523|PEO@GFC-15|Li cell at 0.5C. (i) Rate performance of the NCM523|PEO@GFC-15|Li cell.

g^{-1}. As shown in Fig. 6b, the LFP|PEO@GFC-15|Li cell delivers an initial discharge specific capacity of 151.3 mAh g^{-1} at 0.1C. After 100 cycles, the discharge specific capacity is maintained at 109.1 mAh g^{-1}, with a capacity retention rate of 72.1%, demonstrating good cycling stability. In addition, the LFP|PEO@GFC-15|Li cell also presents a stable interface during cycling, as evidenced by minimal voltage hysteresis and a flat voltage plateau across various cycles (Fig. 6c).

LFP|PEO@GFC-0|Li, LFP|PEO@GFC-10|Li, and LFP|PEO@GFC-20|Li cells display poor cycling stability (Fig. 6d–f). The discharge specific capacities are 24.9, 71.9, and 106.6 mAh g^{-1} after 100 cycles at 0.1C, respectively. The corresponding capacity retention rates are 14.6%, 42.3%, and 62.7%, respectively. These cells show a higher initial discharge specific capacity, but the discharge specific capacity declines dramatically with cycling. This is mainly due to the poor thermal stability of PEO. During long-term cycling, the ether oxygen atoms (–O–) in the polymer backbone are prone to oxidation, resulting in the formation of electron-withdrawing groups such as –CO–, –O–O–, and –COOH. These groups decrease the electron density of adjacent carbon atoms through both inductive and resonance effects, leading to an increase in C–H bond polarity. This promotes the dissociation of H^+ from the PEO backbone, weakening the C–H bond. The dissociated H^+ then reacts with $TFSI^-$ to form HTFSI.[42] HTFSI possesses high corrosivity toward PEO and LFP, accelerating the degradation of the LFP/CSE interface and thereby causing a deterioration in cell performance. In contrast, PEO@GFC-15 can fix $TFSI^-$ on the PEO chain, and abundant LiF can capture H^+, thus minimizing HTFSI generation and forming low-resistance and stable PEO@GFC-15/LFP interfaces.[43,44] Furthermore, XPS analysis indicates that the incorporation of LALZTO and GFC significantly enhances the peak intensity and width of C–H bonds, effectively inhibiting bond cleavage, slowing H^+ dissociation, and reducing the formation of HTFSI. Moreover, benefiting from rapid Li^+ transport capability, electrochemical stability, flexibility, and Li dendrite growth suppression capability, PEO@GFC-15 notably improved the electrochemical performance of SSLBs.

To evaluate PEO@GFC-15 with high-voltage cathodes, NCM523|PEO@GFC-15|Li cells were assembled. The cell was activated over 5 cycles at 0.1C, delivering a stable discharge capacity of 175 mAh g^{-1} (Fig. 6(g and h)). After 26 cycles, the discharge specific capacity remains 100.4 mAh g^{-1} at 0.5C, with coulombic efficiency of 99%. As shown in Fig. 6i, the NCM523|PEO@GFC-15|Li cell exhibits good rate performance. The discharge specific capacities are 173.4, 127.8, and 100.6 mAh g^{-1} at 0.1, 0.2, and 0.5C, respectively. Upon reverting to 0.1C, the discharge specific capacity recovered to 171.3 mAh g^{-1}.

4. Conclusions

In summary, PEO@GFC-15 with rapid Li^+ transport capability, wide electrochemical window, good flexibility, and interface stability was prepared by a simple and scalable solution casting method. LALZTO can enhance the Li^+ transport capability by reducing PEO crystallinity, creating a dynamic Li–O–C coordination network, and generating more free Li^+. The ionic conductivity, migration activation energy, and Li^+ transference number of PEO@GFC-15 are improved to 2.89×10^{-5} S cm^{-1}, 0.50 eV, and 0.793, respectively. LALZTO can also enhance electrochemical stability by promoting LiTFSI decomposition to form abundant LiF and fixing $TFSI^-$ on the PEO chain. The oxidation potential of PEO@GFC-15 is increased to 5.2 V. Moreover, the high elastic modulus of GFC and the strong hydrogen bond network endow PEO@GFC-15 with good flexibility. The three-dimensional rigid network and non-flammable inorganic LALZTO particles can improve the thermal stability of PEO@GFC-15. Benefiting from those advantages, a high CCD of 0.9 mA cm^{-2} and a long cycle life of 500 h at 0.1 mA cm^{-2} were realized for the Li|PEO@GFC-15|Li cell, displaying excellent Li plating/stripping stability. The LFP|PEO@GFC-15|Li cell also shows impressive electrochemical performance. The initial specific discharge capacity is 151.3 mAh g^{-1} and decreases to 109.1 mAh g^{-1} after 100 cycles at 0.1 C. This work effectively enhances the CSE and battery performance by a rigid support–molecular regulation–interface reinforcement synergistic modification strategy, providing a theoretical basis and experimental support for the development and application of SSLBs.

Author contributions

Yingtai Zhao: conceptualization, methodology, investigation, formal analysis, writing – original draft, writing – review & editing. Xiangping Feng: conceptualization, methodology, investigation, formal analysis, writing – original draft, writing – review & editing. Xin Sun: formal analysis, writing – original draft, writing – review & editing. Lei Zhang: conceptualization, investigation, methodology, supervision, writing – original draft, writing – review & editing. Zhishuang Song: formal analysis, writing – original draft, writing – review & editing. Jinzhu Zhao: formal analysis, writing – original draft, writing – review & editing. Zhiyuan Wang: formal analysis, writing – original draft, writing – review & editing. Runguo Zheng: conceptualization, investigation, methodology, supervision, writing – original draft, writing – review & editing. Hongyu Sun: conceptualization, investigation, methodology, supervision, writing – original draft, writing – review & editing. Yanguo Liu: conceptualization, investigation, methodology, supervision, writing – original draft, writing – review & editing.

Conflicts of interest

The authors declare that they have no known competing financial interests or personal relationships that could have appeared to influence the work reported in this paper.

Data availability

The data supporting this article have been included as part of the SI. This supporting information file provides comprehensive supplementary data and literature comparisons for the manuscript titled "Rigid Support-Molecular Regulation-Interface Reinforcement Synergistic Strategy Enables PEO-Based Electrolytes for Solid-State Lithium Batteries." The file includes five supplementary figures (Fig. S1–S5) and three supplementary tables (Tables S1–S3). The figures present the physical morphology, electrochemical impedance spectra, flexibility tests, thermal stability analyses, and X-ray diffraction (XRD) patterns of electrolytes with varying compositions. The tables offer a detailed comparison of key properties, including ionic conductivity, activation energy, lithium-ion transference number, oxidation potential, and battery cycling performance, for a range of PEO-based electrolytes. Furthermore, the optimal sample, PEO@GFC-15, is compared with strategies reported in recent literature. Additionally, 15 relevant references are cited to further substantiate the effectiveness and advanced nature of the synergistic strategy proposed in this work, particularly in enhancing the electrochemical performance and interfacial stability of PEO-based solid-state electrolytes. See DOI: **https://doi.org/10.1039/d5nr02999f**.

Acknowledgements

This study was financially supported by the National Natural Science Foundation of China (no. 52471068, 52177208, 52171202), the Hebei Natural Science Foundation (no. E2024501016, E2023208051), and Fundamental Research Funds for the Central Universities (N2423008).

References

1 L. Zhang, Y. Dai, C. Li, Y. Dang, R. Zheng, Z. Wang, Y. Wang, Y. Cui, H. Arandiyan, Z. Shao, H. Sun, Q. Zhuang and Y. Liu, *Energy Storage Mater.*, 2024, **69**, 103378.
2 L. Zhang, Q. Zhuang, R. Zheng, Z. Wang, H. Sun, H. Arandiyan, Y. Wang, Y. Liu and Z. Shao, *Energy Storage Mater.*, 2022, **49**, 299–338.
3 S. Luo, N. Deng, H. Wang, Q. Zeng, Y. Li, W. Kang and B. Cheng, *Chem. Eng. J.*, 2023, **474**, 145683.
4 D. Li, D. Zhang, Y. Ma, X. Yang, J. Xu, X. Zheng, P. Shen, S. Xu, Y. Xiong, Y. Gong, M. Liu, Y. Wang, Z. Shen and Y. Hu, *Nano Energy*, 2025, **141**, 111136.
5 Q. Li, F. Tian, L. Lu, Q. Lv, X. Shang, Z. Li and M. Wu, *J. Power Sources*, 2025, **641**, 236900.
6 H. Zhang, F. Lian, L. Bai, N. Meng and C. Xu, *J. Membr. Sci.*, 2018, **552**, 349–356.
7 X. Fu, C. Li, Y. Jewel, Y. Wang, J. Liu and W. Zhong, *ECS Meeting Abstracts*, 2018, **MA2018-01**, 415–415.
8 W. Liu, L. Meng, X. Liu, L. Gao, X. Wang, J. Kang, J. Ju, N. Deng, B. Cheng and W. Kang, *J. Energy Chem.*, 2023, **76**, 503–515.
9 Y. Huang, Y. Cheng, H. Zhang, L. Mai and L. Xu, *Chem. Eng. J.*, 2023, **470**, 144120.
10 X. Hu, M. Jing, H. Yang, Q. Liu, F. Chen, W. Yuan, L. Kang, D. Li and X. Shen, *J. Colloid Interface Sci.*, 2021, **590**, 50–59.
11 X. Chen, C. Liu and W. Aftab, *Nano Res. Energy*, 2023, **3**, 90–91.
12 F. Wu, A. Mullaliu, T. Diemant, D. Stepien, T. N. Parac-Vogt, J.-K. Kim, D. Bresser, G.-T. Kim and S. Passerini, *InfoMat*, 2023, **5**, 12462.
13 M. Zhang, F. Makhlooghiazad, U. Pal, M. Maleki, S. Kondou, G. A. Elia, C. Gerbaldi and M. Forsyth, *ACS Appl. Polym. Mater.*, 2024, **6**, 14469–14476.
14 C. Song, J. Gao, H. Shen, Z. Wang, F. Li and G. Li, *Chem. Eng. J.*, 2025, **511**, 162077.
15 Y. Li, P. Ding, L. Cai, L. Shi, Y. Zhao, H. Liu, H. Yuan, D. Yu, C. Guo, Q. Gao, L. Li, Y. Ren, C. Nan and Y. Shen, *Adv. Energy Mater.*, 2025, **11**, 774.
16 Y. Chen, W. Zhao, Q. Zhang, G. Yang, J. Zheng, W. Tang, Q. Xu, C. Lai, J. Yang and C. Peng, *Adv. Funct. Mater.*, 2020, **30**, 396.
17 L. Zhang, S. Cao, Y. Zhang, C. Zhang, P. Guo, J. Song, Z. Jiang and C. Shi, *Chem. Eng. J.*, 2024, **479**, 147764.
18 Y. Zheng, Y. Shen, J. Guo, J. Li, J. Wang, D. Ning, Y. Liu, Y. Huang, Y. Tang, Y. Deng, H. Yan and H. Shao, *Nano Res. Energy*, 2024, **3**, 9120118.
19 X. Zhang, S. Cheng, C. Fu, G. Yin, L. Wang, Y. Wu and H. Huo, *Nano-Micro Lett.*, 2024, **17**, 2.
20 Z. Cheng, T. Liu, B. Zhao, F. Shen, H. Jin and X. Han, *Energy Storage Mater.*, 2021, **34**, 388–416.
21 D. D. Sloovere, J. Mercken, J. D'Haen, E. Derveaux, P. Adriaensens, P. M. Vereecken, M. K. V. Bael and A. Hardy, *Adv. Sci.*, 2024, **11**, 583.
22 X. Feng, L. Zhang, C. Li, M. Shen, R. Zheng, Z. Wang, H. Sun and Y. Liu, *Ceram. Int.*, 2024, **50**, 38999–39009.
23 L. Zhang, Q. Meng, Y. Dai, X. Feng, M. Shen, Q. Zhuang, Z. Ju, R. Zheng, Z. Wang, Y. Cui, H. Sun and Y. Liu, *Nano Energy*, 2023, **113**, 108573.
24 C. Bao, C. Zheng, M. Wu, Y. Zhang, J. Jin, H. Chen and Z. Wen, *Adv. Energy Mater.*, 2023, **13**, 2204028.
25 T. Jiang, P. He, G. Wang, Y. Shen, C.-W. Nan and L.-Z. Fan, *Adv. Energy Mater.*, 2020, **10**, 1903376.
26 J. Sheng, S. Zhou, Z. Yang and X. Zhang, *Langmuir*, 2018, **34**, 3678–3685.
27 Y. Ye, Y. Li, J. Wang, S. Yuan, X. Xu, X. Zhang, J. Zhou, B. Wang and X. Ma, *Langmuir*, 2022, **38**, 3265–3275.
28 G. Yao, S. Xiao, Y. Qian, T. Liu, Y. Shi, Y. Zhang, J. Chen and X. Zhou, *Chem. Eng. J.*, 2024, **496**, 153924.
29 Q. Shu, G. Tang, F. Liu, W. Zou, J. He, C. Zhang and L. Zou, *Fuel*, 2017, **209**, 290–298.
30 J.-F. Liu, Z.-Y. Wu, F. J. Stadler and Y.-F. Huang, *Angew. Chem., Int. Ed.*, 2023, **62**, 242.
31 T. Yang, J. Lou, L. Hu, Q. Liu, Z. Huang, Q. Zhou, H. Zhang, W. Song, H. Huang, Y. Wang, X. Tao, Y. Xia, W. Zhang and J. Zhang, *Adv. Funct. Mater.*, 2024, **23**, 719.
32 M. Wang, Z. Peng, W. Luo, F. Ren, Z. Li, Q. Zhang, H. He, C. Ouyang and D. Wang, *Adv. Energy Mater.*, 2019, **70**, 34.

33 S. Tan, Y. Jiang, S. Ni, H. Wang, F. Xiong, L. Cui, X. Pan, C. Tang, Y. Rong, Q. An and L. Mai, *Natl. Sci. Rev.*, 2022, **9**, 11.
34 M. Wang, Z. Peng, W. Luo, F. Ren, Z. Li, Q. Zhang, H. He, C. Ouyang and D. Wang, *Adv. Energy Mater.*, 2018, **29**, 12.
35 J. Su, M. Pasta, Z. Ning, X. Gao, P. G. Bruce and C. R. M. Grovenor, *Energy Environ. Sci.*, 2022, **15**, 3805–3814.
36 D. Shen, W. Liang, X. Wang, L. Yue, B. Wang, Y. Zhou, Y. Yu and Y. Li, *Energy Storage Mater.*, 2024, **72**, 103709.
37 Y. Guo, D. Wu, Z. Sun, F. Ning, K. Zhu, X. Liu, S. Lu, Y. Xia and J. Yi, *J. Phys. Chem. Lett.*, 2025, **16**, 1415–1423.
38 M. Shi, C. Lei, H. Wang, P. Jiang, C. Xu, W. Yang, X. He and X. Liang, *Angew. Chem., Int. Ed.*, 2024, **7**, 261.
39 T.-B. Song, Z.-H. Huang, X.-R. Zhang, J.-W. Ni and H.-M. Xiong, *Small*, 2023, **19**, 2205558.
40 S. Song, Y. Gao, L. Cao, H. S. Park, Z. Liu, F. He, W. Li, M. Liu and P. Yang, *J. Colloid Interface Sci.*, 2025, **695**, 137589.
41 L. Zhang, N. Wang, J. Wang, Y. Dang, R. Zheng, Z. Wang, J. Jiang, Y. Cui, Y. Wu, H. Sun, Q. Zhuang, Y. Liu and X. Sun, *Mater. Today*, 2025, **87**, 77–89.
42 S. Wu, J. Bao, H. Bie and Y. Liu, *Fuel*, 2024, **373**, 132345.
43 H. Xiang, L. Gao, D. Shi, L. Jiao, B. Cheng, N. Deng, G. Li and W. Kang, *Adv. Fiber Mater.*, 2024, **6**, 883–899.
44 Z. Wang, T. Chen, Y. Liu, J. Xing, A. Zhou, J. Li, W. Zou and F. Zhou, *Chem. Eng. J.*, 2022, **430**, 132970.